



<http://www.diva-portal.org>

Postprint

This is the accepted version of a paper published in *European Journal of Pharmaceutical Sciences*. This paper has been peer-reviewed but does not include the final publisher proof-corrections or journal pagination.

Citation for the original published paper (version of record):

Persson, A., Frenning, G. (2013)

The influence of rolling friction on the shear behaviour of non-cohesive pharmaceutical granules: An experimental and numerical investigation.

European Journal of Pharmaceutical Sciences, 49(2): 241-250

<http://dx.doi.org/10.1016/j.ejps.2013.02.022>

Access to the published version may require subscription.

N.B. When citing this work, cite the original published paper.

Permanent link to this version:

<http://urn.kb.se/resolve?urn=urn:nbn:se:uu:diva-204131>

The influence of rolling friction on the shear behaviour of non-cohesive pharmaceutical granules – an experimental and numerical investigation

Ann-Sofie Persson and Göran Frenning*

Uppsala University, Department of Pharmacy, Uppsala Biomedical Centre, P.O. Box 580, SE-751 23 Uppsala, Sweden.

*Corresponding author:

E-mail: Goran.Frenning@farmaci.uu.se, Fax: +46 18-471 42 23, Phone: +46 18-471 43 75

Granule shear behaviour was investigated experimentally and numerically to evaluate the reliability of the numerical model. Additionally, parameters affecting the ensuing flow regimes – elastic quasi-static and inertial non-collisional – were highlighted. Furthermore, the influence of using the Lees–Edwards periodic boundary conditions or the standard boundary conditions was studied. Experiments were performed with microcrystalline cellulose granules of three size distributions using the FT4 powder rheometer. The numerical parameters, particle size, effective density, and particle stiffness were selected to match the experimental conditions.

Experimentally, an unexpected particle size effect was evident where the resistance to shear increased with particle size. Numerically, combining rolling friction and increased shear rate enabled a transition from the inertial non-collisional to the elastic quasi-static regime at a reduced sliding friction coefficient. Presumably, this is an effect of increased particle overlap creating stronger contacts and facilitating force chain formation. Both boundary conditions provided comparable results provided a correction of system size was made, where larger systems were required for the standard boundary conditions. A satisfactory qualitative agreement between the experimentally and numerically determined yield loci emphasised the predictive capacity of the DEM. Rolling friction was in addition concluded to be an essential model parameter for obtaining an improved quantitative agreement.

1. Introduction

The interparticle frictional (Hirano, 2006) and van der Waals forces (Castellanos, 2005; Krupp, 1967) greatly influence the flowability of a dry powder system. Frictional forces dominate for granular materials as cohesive forces may be considered negligible due to the large impact of gravity. The importance of the interparticle friction forces during flow may be characterised by numerical modeling which is an important and powerful tool utilised in the pharmaceutical area (Ketterhagen et al., 2009). The discrete element method (DEM) (Cundall and Strack, 1979) has been used extensively to investigate flowability of powders and granular materials (Aarons and Sundaresan, 2006; Bierwisch et al., 2009; Datta et al., 2008; Zhou et al., 2001). Interesting findings have been obtained by shear simulations with the DEM, e.g. underpinning the concept of flow regimes for granular materials (Campbell, 2002), where the major regimes are the elastic (slow) and the inertial (rapid) flow. The flow regimes are commonly divided into two elastic and two inertial sub-regimes. The elastic regime is divided into the elastic quasi-static and the elastic-inertial regimes depending on the shear-rate dependence during shear. The elastic sub-regimes are characterised by the formation, rotation and breakage of force chains in the granular bed during shear. The difference is manifested by the shear-rate independence in the elastic quasi-static regime and the shear-rate dependence in the elastic-inertial regime. The former regime is most frequently observed in granular flows as unrealistically high shear rates are required to induce inertial effects in the force chain formation (Campbell, 2002). The inertial regime is divided into the inertial non-collisional and inertial-collisional flow regimes in which no force chains are present. The inertial flow regimes are instead characterised by particle collisions, either cluster collisions as in the inertial non-collisional regime or binary particle collisions as in the inertial-collisional regime. Although the inertial flows are considered rapid the subsequent

flow regimes may occur at a slow shear rate provided that shearing takes place at a sufficiently low filling fraction (Campbell, 2002). Transitions between the various flow regimes are enabled by changes in filling fraction and shear rate and may be followed in the flow regime maps for constant volume (Campbell, 2002) and constant applied stress (Campbell, 2005).

Performing DEM simulations of powder systems that are comparable to experimental conditions is a challenging task and often simplified models are used to reduce possible limitations such as computational time. This may however be a drawback regarding the agreement to experimental data. A quantitative correspondence between experiments and simulations when describing complex shearing procedures is best achieved when three-dimensional models are utilized (McCarthy et al., 2010; Tykhoniuk et al., 2007). Furthermore, the inclusion of e.g. correct particle geometric shape (McCarthy et al., 2010), rolling and sliding friction (Ji et al., 2009), and correct initial powder bed porosity (Hartl and Ooi, 2008) has been highlighted as important for increased quantitative agreement to experimental data.

In this work shear of a relatively simple pharmaceutical system was investigated both experimentally and numerically. In the experiments the shearing was conducted at constant applied stress whereas constant volume conditions for simplicity were applied numerically. This may appear to be inconsistent and indeed stated as such by Campbell (2005). However, according to Aarons and Sundaresan (2008), the shear is independent of shearing conditions as stresses scale with e.g. shear rate in a similar manner during both constant applied stress and constant volume conditions. The effects of the various shearing conditions were therefore considered

negligible for the outcome of the study. As a model system we use nearly spherical granules composed of microcrystalline cellulose (MCC) of three size distributions. The simplicity of the system depends on the free flowing properties of the granules and the absence of cohesive forces which assures no formation of secondary agglomerates. This facilitates the selection of parameters used in the DEM simulation, some of which were selected from an earlier work (Persson et al., 2011) on granule flowability. The major objective of this work was to investigate the effect of rolling friction on the shear behaviour of non-cohesive granules, as manifested by transitions between flow regimes. This was made in conjunction with a systematic alteration of the sliding friction coefficient in order to acquire a deeper insight of the complete granule shear behaviour. Prior investigations have addressed the effects of cohesion (Aarons and Sundaresan, 2006, 2008) and particle shape (Campbell, 2011) on the flow-regime transitions whereas the effect of rolling friction appears not to have been studied in detail. An additional objective was to assess the effects of boundary conditions and system size on the shear behaviour. To this end, simulations with the traditionally used Lees-Edwards periodic boundary conditions were compared with simulations using the standard boundary conditions. The final objective was to appraise the potential of DEM to describe granule shear by an experimental and numerical comparison. This was performed in an attempt to contribute to an improved knowledge of important model parameters necessary for increased quantitative agreement and thereby taking a step towards a predictive tool suitable for utilisation in the pharmaceutical formulation development.

2. Materials and methods

2.1 Materials

Spherical MCC granules of three size distributions (Cellets[®] 100 (100-200 μm), Cellets[®] 200 (200-355 μm), and Cellets[®] 350 (350-500 μm)) were obtained from HARKE Pharma GmbH, Germany. The granules are hereafter referred to as C100, C200, and C350. The apparent particle density (number of independent measurements, $n=2$) of MCC (1.57g/cm^3) was measured with helium pycnometry (AccuPyc 1330, Micromeritics, USA). The granules were stored at room temperature above a saturated solution of K_2CO_3 giving a relative humidity (RH) of approximately 40% for a minimum of 5 days before any measurements were performed.

2.2 Experimental methods

2.2.1. Granule characterisation

External volume specific surface area: Steady-state permeametry was used for assessment of the granule external volume specific surface area ($n=3$). The granules were manually poured into a cylinder (11.47mm diameter) and the height of the granule bed was measured (Mitutoyo Digimatic, ID-C, Tokyo, Japan). Controlled air flow was connected to the granule bed and the generated pressure was recorded (P 200 S, Digitron Instrumentation Ltd, UK) from high to low flow rate. The pressure was used for calculation of the surface area as described earlier (Eriksson et al., 1993) using the Kozeny-Carman equation and an aspect factor of 6.

Median particle size: The particle size distribution of C200 and C350 was determined in a previous work (Persson and Frenning, 2012) using a flatbed scanner. The same method was

however not usable for the C100 granules due to limitations in the image resolution (1600 dpi). Instead, an average surface-volume shape factor of ~ 6.8 was calculated from the known median particle size and external volume specific surface area of C200 and C350. As the various granules comprise the same raw material and are similarly manufactured the granules are expected to possess similar properties regarding e.g. shape and porosity. The surface-volume shape coefficient was hence assumed to be the same for C100 as for C200 and C350 and the median particle size was therefore calculated from the measured volume specific external surface area.

Mercury pycnometry: The effective granule density ($n=2$) was assessed from mercury pycnometry (Autopore III 9420, Micromeritics, USA) as described by Wikberg and Alderborn (1990).

Bulk and tap densities: The granule bulk density (ρ_{bulk}) ($n=3$) was measured as described in (Persson et al., 2011) by manually pouring granules (39-43 g) through a funnel into a measuring cylinder (50 mL and 21.35 mm diameter) and weighing (Delta Range B3002, Mettler Toledo, Switzerland). The pellet volume was considered sufficient as the cylinder diameter to particle diameter ratio was exceeding 40 for the largest granule size (350-500 μm). The influence of wall effects on the subsequent volume readings was thus assumed to be negligible. The granule bed was subsequently tapped (PharmaTest PT-TD, Hainburg, Germany) to assess the tapped bulk density (ρ_{tap}). No significant volume difference was observed after 150 taps and consequently 500 taps were considered sufficient for a correct determination of the tapped density.

2.2.2 Flowability characterisation

Carr's compressibility index: Carr's compressibility index (CI) ($n=3$) (Carr, 1965) was calculated in the standard manner from the bulk and tap densities as $CI = (\rho_{\text{tap}} - \rho_{\text{bulk}})/\rho_{\text{tap}}$.

Shear: The shear properties of the materials were measured as the stress required to cause powder failure. A FT4 powder rheometer (Freeman Technology Ltd., Worcestershire, UK) with a rotational shear head (24 mm diameter) equipped with 18 vertical blades was used in the shear measurements. These were performed in a 10 mL sample holder (25 mm diameter) of borosilicate glass. Prior to the shear tests, conditioning with a five degree positive helix shaped blade (23.5 mm diameter) was performed in accordance to the instrument original settings to assure a standardised packing of the granule bed and to remove possible effects of differences in powder handling. During the shear tests an initial pre-consolidation of the granule bed to 9 kPa was performed with a stainless steel vented piston, after which the sample holder was split thus giving a sample volume of 10 mL. Secondly, pre-shear was conducted at a normal stress of 9 kPa to reach steady-state. During initial pre-shear a maximum shear stress was detected and then steady-state was approached during 20s from which the pre-shear stress was chosen as the average of the last 10% of the steady-state condition. Finally, the shear tests ($n=3$) were performed from high to low normal stress (7, 6, 5, 4, 3 kPa) at a rate of 18°/min to determine the incipient yield locus. Note that the pre-shearing procedure was repeated in between the shear tests at the applied normal stresses to assure steady-state. The points constituting the yield locus were selected as the maximum shear stress causing failure at each normal stress (incipient failure) or the average value of the last 10% of steady-state (continuous flow, same as for pre-shear). The effective yield

locus (Fig. 1) indicating the steady-state flowability for a non-cohesive material was set as the line passing through the origin and tangent to the large Mohr circle (the circle that touches the incipient yield locus at the largest shear to normal stress ratio) (Nedderman, 1992). The data were analysed with the Data analysis software version 3.01.0063 provided by Freeman Technology.

In order to reduce effects of scattering during measurements, the prorated shear stress (τ_{pro}) was calculated and henceforth used as the measured shear stress. Prorating corrects for scatter in the pre-shear phase according to (European Federation of Chemical Engineering, 1989),

$$\tau_{\text{pro}} = \tau_{\text{shear}} \frac{\overline{\tau_{\text{pre}}}}{\tau_{\text{pre}}}, \quad (1)$$

where τ_{shear} is the shear stress, $\overline{\tau_{\text{pre}}}$ is the average pre-shear shear stress, and τ_{pre} is the pre-shear shear stress assuring the shear plane to be in steady-state. The yield locus (Fig. 1) provided by the shear vs. normal stress data was used to estimate the cohesion (τ_c), the internal (μ_i) and the effective (μ_e) friction coefficients from the intercept and slope of the incipient yield locus, and the slope of the effective yield locus, respectively.

2.3 Numerical method

2.3.1 Contact model

In this work, a contact model of the linear spring dashpot (LSD) type was used, as has been done in a number of previous investigations (Aarons and Sundaresan, 2006; Campbell, 2002; Ji et al., 2009; Silbert et al., 2001). The elastic parts of the normal and tangential forces (F_n and F_t) were

hence assumed to be proportional to the normal and tangential overlaps (\mathbf{u}_n and \mathbf{u}_t) whereas the viscous parts were proportional to the normal and tangential velocities (\mathbf{v}_n and \mathbf{v}_t):

$$\mathbf{F}_n = -(k_n \mathbf{u}_n + c_n \mathbf{v}_n), \quad (2)$$

$$\mathbf{F}_t = -(k_t \mathbf{u}_t + c_t \mathbf{v}_t). \quad (3)$$

Both the normal and tangential stiffness (k_n and k_t) were selected as 50 N/mm for the particle–particle contacts, and the normal and tangential damping coefficients (c_n and c_t) were chosen so that the fractional damping was 0.3 (see (Persson et al., 2011)).

The tangential force was truncated in accordance with normal Coulomb friction, so that

$$|\mathbf{F}_t| \leq \mu_s |\mathbf{F}_n|, \quad (4)$$

where μ_s is the sliding friction coefficient. Rolling friction was included in the model, as suggested by Zhou et al. (1999), and the rolling torque was expressed as

$$\mathbf{T}_r = -\mu_r R |\mathbf{F}_n| \hat{\boldsymbol{\omega}}, \quad (5)$$

where μ_r is the rolling friction coefficient, R is the particle radius and $\hat{\boldsymbol{\omega}}$ is a unit vector pointing in the same direction as the angular velocity. Notice that the radius has been included in the defining equation of the rolling torque in order to make the rolling friction coefficient non-dimensional.

2.3.2 Simulations

In all simulations, monodisperse spherical particles with diameter 0.425 mm and effective density 1.45 g/cm^3 were used. Simulations were performed for varying sliding and rolling friction coefficients (μ_s and μ_r), and whenever confining surfaces were included in the simulation domain (see below), the values of μ_s and μ_r for the particle–wall interactions were chosen as 60% of the values assigned to the particle–particle interactions. As suggested by Campbell (2002), the time step was selected as 1/50 of the binary collision time.

All simulations were performed in a rectangular domain with side-length L in the x and y directions and height H in the z direction (Fig. 2). The geometry was such that the velocity gradient was in the z direction and the streaming velocity in the y direction. Two types of boundary conditions (BCs) were used.

Firstly, the Lees–Edwards BCs (LEBCs) (Lees and Edwards, 1972), which utilises translated images of the system as illustrated in Fig. 2a. The images above (below) the simulation domain move with velocity $v = \gamma H$ in the positive (negative) y direction, thus maintaining a constant shear rate γ . Any particle that exits the simulation domain in the positive (negative) z direction is reinserted from below (above), as per standard periodic BCs, but with appropriate adjustments made to its velocity and position to account for the relative motion of the images. Standard periodic BCs are employed in the x and y direction, thus resulting in a system without boundaries. Simulations were performed for cubic simulation domains (i.e., $H = L$), with 2000 particles.

Secondly, standard BCs (SBCs), with a stationary base and a moving lid, as illustrated in Fig. 2b. Baffles of height h were used to counteract any relative motion between the base/lid and the granules (h was kept fixed at two particle diameters, i.e., $h = 0.85$ mm). Standard periodic BCs were employed in the x and y direction also in this case. Simulations were performed for three different aspect ratios ($H/L = 1, 2$ and 4), with 2000, 4000 and 8000 particles and representative frictional coefficients, $\mu_s=0.5$ and $\mu_r=0.1$.

Initial particle assemblies for the flow simulations were generated in the following manner. Particles with random initial velocity were regularly positioned in a larger simulation domain (corresponding to filling fractions of 0.25) with periodic BCs in two (for SBCs) or three (for LEBCs) directions. The simulation domain was next reduced in size along all three spatial directions, until the desired filling fraction was reached. For LEBCs, an initial shearing motion of the particles was imposed, so that the initial velocity was in agreement with the mean shear flow. For SBCs, the particles were stationary in the initial state.

Simulations were performed at fixed volume for two different shear rates γ (0.1 and 0.01 ms^{-1}) and all reported stress values are averages obtained during steady state (obtained for times t such that $6 \leq \gamma t \leq 12$). The shear rates used in this study were sufficiently low that streaming stresses were negligible and consequently the reported mean stresses refer to the contact (or collisional) stress. The contact stress tensor is defined as (Aarons and Sundaresan, 2006; Campbell, 2002; Latzel et al., 2000)

$$\boldsymbol{\sigma} = \frac{1}{V} \sum_{i,j} \mathbf{F}_{ij} \otimes \boldsymbol{\ell}_{ij}, \quad (6)$$

where $\mathbf{F}_{ij} \otimes \boldsymbol{\ell}_{ij}$ denotes the tensor product of contact force \mathbf{F}_{ij} (between particles i and j) and branch vector $\boldsymbol{\ell}_{ij}$ (that connects the centres of particles i and j), V is the volume of the simulation domain, and the summation extends over all particle contacts. In addition, when SBCs were used, the normal and tangential forces on the moving lid were sampled and converted into stresses, in the same manner as for an experimental shear cell.

3. Results and discussion

3.1 Experimental study

3.1.1 Granule characteristics

Volume specific external surface area: The difference in particle size was reflected in the measurements of volume specific external surface area where the area decreased with increasing nominal particle size (Table 1).

Median particle size: As previously determined (Persson and Frenning, 2012) the particle size distributions for the C200 and C350 were consistent with the specifications made by the manufacturer ($\geq 85\%$ within the stated range). In addition, the determined median particle size (d_{50}) (Table 1) for the respective granules was found to be larger than the mean particle size calculated from the specified range. The d_{50} for C100 calculated by using the surface-volume

shape coefficient was also larger than the corresponding mean particle size, indicating that consistent values of d_{50} were obtained by the method used.

Mercury pycnometry: As expected the effective granule density (Table 1) could be regarded as equal for the various granules due to the same preparation method. In addition, granules manufactured from MCC and water generally tend to be of low porosity (Johansson et al., 1995) which also was obtained from calculations of the granule porosity as one minus the ratio between the effective and apparent densities (yielding porosities ~7%).

Bulk and tapped densities: The spontaneous granule packing density tended to increase with increased particle size as indicated by the poured bulk densities (Table 1). However, the tapped bulk densities displayed the same close granule packing independent of granule size. The small increase in bulk density with tapping indicated that the granules were arranged in a close manner already after pouring which is dependent on the spherical shape and relatively large particle size.

3.1.2 Flowability properties

Carr's compressibility index: It is well known that flowability generally improves with increasing particle size and the expected trend was visible from the calculated Carr's compressibility index (Table 1). Despite the differences in CI between C100 and the larger granules all granule types were classified as excellent flowing (Carr, 1965).

Shear: Inversely to the CI, the position of the yield locus from the shear data categorised the flowability properties in the order of C350, C200 and C100 where the small granules possessed best flowability. The same trend was observed independent of whether data collection was made from the maximum (Fig. 3a) or the average steady-state (Fig. 3b) shear stress. This categorisation was somewhat unexpected as the interparticle forces tend to be smaller for large particles which ultimately would have a positive effect on the flowability properties.

The incipient shear properties (i.e., shear stress derived from maximum detectable shear stress) are displayed as cohesion (τ_c), internal (μ_i) and effective (μ_e) friction coefficients (Table 2). Although small standard deviations in the yield loci were obtained large spreads in τ (intercept of extrapolated yield locus) were visible. Despite the spread the C350 were less cohesive ($p < 0.05$) than C100 and C200 which is expected as the gravitational force dominates over interparticle forces for large particles (Castellanos, 2005). In addition, notice that the incipient yield loci at zero applied normal stress intercepts the shear stress axis giving a value of the cohesion force present in the system although the measurements were performed on particles with negligible cohesion. This and the large spread in data may however be indicative of the uncertainty in the extrapolation of the data for granular systems and focus will henceforth be on the internal and effective friction coefficients. The μ_i and μ_e indicated a significantly ($p < 0.05$) increased resistance to motion with increased particle size (Table 2). This may possibly be explained by geometrical factors that become apparent for relatively coarse and spherical particles. During shearing the particles will thus experience interlocking at the uneven shear plane. The geometrical factors may also include jamming effects due to a decreased particle bed height to particle diameter ratio with increased particle size. This causes irregular shear planes, thus

resulting in an increased shear resistance for the intermediate and large sized granules (Savage and Sayed, 1984). Furthermore, it may be hypothesised that the size dependence is a kinetic effect as the particle momentum increases with particle size at constant shear rate. Hence, the shear stress increases with particle size in order to induce powder failure. In addition, the μ_i and μ_e are similar for the various granules except for the C100 indicating that the internal and effective friction coefficients provide consistent information for the intermediate and large sized granules, as indeed should be the case for non-cohesive particles.

Similar information was provided from the yield loci derived from the average shear stress of the last 10% of the steady-state condition (Table 3). Significant differences in μ_i and μ_e was although only obtained between the small and intermediate or large sized granules. Comparing the two data collection approaches, similar shear vs. normal stress profiles are visible (compare Fig. 3a and b). However, the generated shear stress collected during steady-state was generally somewhat lower than the maximum detectable shear stress as expected. The internal and effective friction coefficients obtained from the two sampling approaches displayed varying results – for the μ_i difference ($p < 0.05$) between the sampling procedures was only proven for C350 whereas for the μ_e difference was seen for the C100 and C350. Interestingly, this indicates that there may be a difference in the onset of flow and continuous flow of the granules despite that cohesion is negligible in the granular systems.

3.2 Numerical study

Effect of simulation parameters: The generated normal and shear stresses during shearing are known to be dependent on the filling fraction, the sliding friction, and the shear rate (Aarons and Sundaresan, 2006; Campbell, 2002). The influence of rolling friction on the flow regimes is however unclear and therefore investigated in the simulations together with the former parameters. The studied systems were composed of mono-disperse particles and simulated using the Lees–Edwards boundary conditions (LEBCs). The addition of rolling friction to the model was performed to alter the apparent particle shape (Wensrich and Katterfeld, 2012) to capture the behaviour of slightly unspherical particles or particles possessing some surface asperities and hence to create a more realistic model for the granular system.

Initially, simulations were performed at a shear rate of 0.01 ms^{-1} without the incorporation of rolling friction (μ_r). The magnitude and evolution of stress (both normal and shear stress) was influenced by the sliding friction (μ_s) and the filling fraction, where as expected high parameter values contributed to larger stresses (see Fig. 4a for the evolution in shear stress, in which the stress has been scaled elastically by multiplication with the ratio of the particle diameter to the contact stiffness). Additionally, filling fractions above a critical value of approximately 0.58 (for intermediate and high μ_s) were required to induce resistance to motion, whereas flow occurred freely for filling fractions below this critical value. This finding is expected as intuitively a denser particle packing and an increased resistance to sliding (possibly causing mechanical interlocking (Savage and Sayed, 1984)) require larger external stresses to enable particle flow. The inclusion of rolling friction ($\mu_r=0.1$ and $\mu_r=0.2$) had most impact on the stresses generated at low filling fractions although a slight increase in magnitude in addition was observed at denser particle packing (the shear stress is displayed in Fig. 4b). The largest effect of μ_r was elimination of the

critical filling fraction for the intermediate and high μ_s clearly displaying an increased resistance to induce shear due to the rolling interference. Thus, sliding and rolling friction provided supplementary resistance to shear and was required for stable shearing. Similar behaviour was displayed for ellipsoidal particles (Campbell, 2011) which may be considered comparable as studying spheroids with addition of rolling friction (Wensrich and Katterfeld, 2012). The shear behaviour was however virtually independent of the magnitude of the rolling friction coefficients investigated, suggesting that $\mu_r=0.1$ may be considered as a saturation level beyond which small effects are observed. Consequently, the focus will henceforth be directed to the simulations performed with the lower μ_r unless otherwise stated.

A linear correlation was observed for the ratio of shear to normal stress (commonly referred to as the apparent bulk friction) to the filling fraction for low μ_s . For the intermediate and high μ_s instead a correlation with two distinct regions was apparent independently on absence (Fig. 5a) or presence (Fig. 5b) of rolling friction. The latter correlation may be divided into a linear and a steady-state part where generally the linear relationship occurs at low filling fractions and the steady-state correlation is apparent at high filling fractions. The regions may be interpreted as the inertial non-collisional and the elastic quasi-static flow regime, respectively (Campbell, 2002). The former is generally characterised by large cluster collisions and the latter by the presence of force chains supporting the granule bed. The strength of the force chains are affected by the presence and the magnitude of μ_s thus explaining the elastic quasi-static regime for high sliding friction coefficients (Aarons and Sundaresan, 2006). Conversely, the low μ_s is unable to provide strength to the force chains resulting in inertial non-collisional flow during the entire investigated range (Campbell, 2002). In addition, the flow regime transition is known to be dependent on the

filling fraction. The critical filling fraction, i.e. the filling fraction where the flow regime transition occurs, was determined from the intersection of two independent linear regression lines (Table 4). Visual inspection of the data obtained without rolling friction (Fig. 5a) suggested that the critical filling fraction was between 0.59 and 0.60 for $\mu_s = 0.3$ and between 0.58 and 0.59 for $\mu_s \geq 0.5$. For $\mu_s = 0.3$, the inertial non-collisional and the elastic quasi-static regression lines were hence determined for filling fractions ≤ 0.59 and ≥ 0.60 , respectively. For $\mu_s \geq 0.5$, the regression lines were analogously determined for filling fractions ≤ 0.58 and ≥ 0.59 . The same regions were applied to the data obtained with rolling friction (Fig. 5b) to enable an unbiased comparison. As expected the critical filling fraction decreased with increasing sliding and rolling friction coefficients.

Shear rate in combination with rolling friction (μ_r) had a major impact on the generated stresses, especially at low filling fraction. The effect of varying shear rate was manifested as a parallel shift in the shear stress vs. filling fraction curve (Fig. 6). Hence, increasing the shear rate from 0.01 ms^{-1} to 0.1 ms^{-1} in presence of μ_r increased the stresses between three to seven folds for the lowest filling fraction and intermediate to high μ_s (Fig. 6 display the $\mu_s=0.7$ and $\mu_r=0.1$ simulations). Additionally, the internal friction coefficients (μ_i) i.e. the slope of the yield loci displayed clearly a shear rate dependence. For the slowly sheared systems ($\dot{\gamma}=0.01 \text{ ms}^{-1}$) the μ_i gradually increased with increased sliding friction reaching a maximal value slightly above 0.35 (Fig. 7a). Addition of μ_r increased the shear resistance marginally for the low μ_s but the resistance remained unchanged for the intermediate and high μ_s . Increasing the shear rate to 0.1 ms^{-1} resulted interestingly in similar results for $\mu_r=0$ but for systems including rolling friction a plateau at the maximal μ_i was reached already at $\mu_s=0.3$ (Fig. 7b). The apparent bulk friction (Fig. 5 and

corresponding data for $\dot{\gamma}=0.1 \text{ ms}^{-1}$) suggests a critical sliding friction coefficient, beyond which the transition to the elastic quasi-static regime occurs. Utilising the critical μ_s it is proposed that a corresponding internal friction limit may be used to distinguish the inertial non-collisional and the elastic quasi-static regime. The limit seems to be independent of shear rate and is apparent at $\mu_i \approx 0.325$, i.e. shearing occurs in the inertial non-collisional regime for $\mu_i < 0.325$ and in the elastic quasi-static regime for $\mu_i > 0.325$. In this context one may note that flow in the elastic-inertial regime instead of the inertial non-collisional regime was considered as this would be possible at a reduced rate for unspherical particles compared to as for spheroids (Campbell, 2011). However, the studied shear rates remain too small for introducing elastic-inertial effects and the flow regime transition was not considered further. From Fig. 7 it is evident that the effect of rolling friction is more pronounced at large shear rate. The effect is however most noticeable at small μ_s whereas for high μ_s the effect of rolling friction is negligible. In addition at sufficiently high μ_s ($\mu_s \geq 0.5$) the sliding friction coefficient appears to have a limited effect on the internal friction coefficient.

For $\mu_s=0.3$ and $\dot{\gamma}=0.1 \text{ ms}^{-1}$ it is implied that the presence of μ_r induced a transition from the inertial non-collisional to the elastic quasi-static regime, displaying once more the additional facilitation of force chain formation in presence of rolling friction. A hypothetical explanation for this regime transition is given as follows. Inclusion of a rolling friction coefficient in a simulated particle system generally causes an increased particle overlap, as confirmed by the simulations (Fig. 8), thereby resulting in a higher contact force. It is conjectured that the increased particle overlap generated particle clusters which remained in contact for a prolonged time as compared to freely rolling systems. In addition it is proposed that the sliding friction coefficient enhanced

the stability of the clusters forming force chains within the cluster that increase in strength with μ_s in a similar manner as the force chains in a granular bed described above. During cluster collision at low shear rate ($\gamma=0.01 \text{ ms}^{-1}$) and μ_s , weak cluster contacts will form and break during shear creating the inertial non-collisional behaviour. Instead at higher μ_s the force chain formation between the clusters was facilitated due to the limited sliding possibility. An improved potential for generation of force chains through the entire granule bed is thus apparent resulting in a transition from the inertial non-collisional to the elastic quasi-static regime. Similar to the inclusion of rolling friction, an increased particle overlap is expected with increased shear rate, which indeed also was observed in the simulations (Fig. 8). The somewhat larger ensuing stresses are seen at low sliding friction ($\mu_s=0.1$ and 0.3) and in absence of rolling friction (compare the filled circles in Fig. 7a and b). The stress increase for the frictionless system at $\gamma=0.1 \text{ ms}^{-1}$ appears to be comparable to the stress increase at $\gamma=0.01 \text{ ms}^{-1}$ in presence of rolling friction (Table 5). Hence, combining the effect of rolling friction and increased shear rate would ultimately result in an enlarged particle overlap, which was supported by the closed diamonds in Fig. 8, and thus enhanced stresses. It is thereby likely that the increased particle contact enabled force chain formation despite low sliding friction. Notice however that the stresses cannot increase indefinitely by changing rolling friction and shear rate as a maximum stress generation (i.e. the plateau in Fig. 7) was observed in the granular bed during flow.

Effect of geometrical configuration and boundary conditions: The majority of the simulations were performed using the LEBCs (Lees and Edwards, 1972) which are often used in shear simulations (Aarons and Sundaresan, 2006; Campbell, 2002) since they are insensitive to fluctuations in system size and provide homogenous shear. In this work simulations were also

made on representative systems ($\mu_s=0.5$ and $\mu_r=0.1$) for three geometrical configurations (cubic and rectangular) with the SBCs. As described in Sec. 2.3.2, the mean contact stress was sampled when LEBCs were used whereas stresses were determined from the forces on the lid for SBCs. Generally, the evolution in both the normal and shear stresses were similar and relatively insensitive to the geometrical configuration and sampling procedure. For the SBCs, small decreases with increasing system size (from cubic ($H/L=1$) to rectangular configurations ($H/L=2$ and 4)) were nevertheless evident at both shear rates studied. However, nearly overlapping results were obtained for the largest system size ($H/L=4$ with 8000 particles) and the LEBCs (2000 particles) (the generated shear stresses are displayed in Fig. 9). In summary, the effect of confining surfaces decreased with increasing system size, but remained also for the largest system, where force chains as long as 50 particle diameters could form. Nevertheless, it is concluded that accurate simulations may be performed independently of type of boundary conditions used provided that a compensation of particle number is taken into account to achieve steady-state shearing. In addition, the CPU-time is essential to take into account were simulations of smaller systems generally require less time to complete.

3.3 Evaluation of DEM

A complete quantitative comparison between experiments and simulations is difficult to perform due to difficulties in experimentally determining individual particle parameters for utilisation in the numerical model. The majority of input parameters were selected from previous experiences on granule flowability where a satisfactory correspondence between experiments and simulations were obtained (Persson et al., 2011) and the parameters were thus considered appropriate to

utilise further. Additionally, it should be noted that the simulated range of filling fractions (0.56-0.62) covers the experimental filling fractions ranging between 0.60-0.61 as determined from the granule bed compressibility at the various applied pressures during shear.

Numerical shear data are commonly elastically scaled with respect to particle stiffness (by multiplication with the ratio of the particle diameter to the contact stiffness). This scaling normalises data with respect to stiffness and is insensitive to changes in both particle diameter and stiffness (Campbell, 2006). Hence, the shear stress data will not change with particle size for non-cohesive particles. It was therefore considered adequate to compare the experimental and numerical data for one of the granular systems. In this work the comparison was performed for the relation between the shear and normal stresses i.e., the yield locus, using the C350 granules. The yield locus generated dimensionless quantities suitable for comparison as significantly larger stresses were obtained in the simulations compared to in the experiments (MPa vs. kPa). This indicates that the particle stiffness was overestimated when determined from the plastic part of the force-displacement correlation during single granule compression (Persson and Frenning, 2012).

A qualitative correspondence in yield loci was obtained between experiments and LEBCs simulations (Fig. 3 and 10) with a nearly linear positive correlation between shear and normal stress. However, the internal friction coefficients calculated from the slopes of the yield loci are higher for the experimental data (compare Table 3 and 5). As observed from Fig. 10 a somewhat steeper slope may be indicated at low stresses suggesting that an increased resemblance to

experiments is possible at low filling fractions. Calculations of these internal friction coefficients indeed confirm the observation and display approximately 2-38% higher values compared to the internal friction coefficients given in Table 5. The largest deviations were apparent for the low sliding friction coefficients. At these filling fractions, the data however indicate that the internal friction coefficients decrease with increased sliding friction in presence of rolling friction which appears counterintuitive. As the deviations were apparent below the critical filling fraction the shearing occurred in the inertial non-collisional regime, hence explaining the generation of higher stresses at low filling fractions. Thus, the internal friction coefficients derived from the complete linear yield loci ($R^2 > 0.993$) were considered representative for the simulated system and used in the comparison. From the results described above it is obvious that the parameters studied – sliding friction, rolling friction and shear rate – influenced the correspondence to experimental data. The effect of rolling friction was much dependent on the sliding friction parameter and was more pronounced for the low sliding friction coefficients as displayed in Fig. 7. It is however clear that the presence of rolling friction enhanced the shear resistance and is an important parameter in order to resemble the experimental system (Ji et al., 2009; Persson et al., 2011) which was expected as the experimental granules are not perfect spheres (surface-volume shape factor ~ 6.8).

The three system sizes (obtained by changing shear cell geometry) simulated with the SBCs may be considered as representative for granular systems with varying particle size (decreases with increased particle bed height) and thereby comparable to the three experimental systems. The resulting yield loci displayed an independence of system size and hence also particle size. This may appear contradictory as indeed a size effect is observed in Fig. 9. However, the evolution in

normal stress (data not shown) was similar to the one for the shear stress providing a yield locus that was insensitive to changes in particle size.

The divergence between experiments and simulations is presumably explained either by the non-spherical granule shape or by the inability to determine some of the included model parameters experimentally. Additionally, there is a possibility that other parameters such as cohesion would have been an important model parameter as suggested by the calculated cohesion parameter (Table 3). Furthermore, one may also consider optimising the shear mechanism (dependent on geometry of shear cell) and shearing rate for an increased experimental resemblance.

4. Conclusions

In this paper, granule shear behaviour was investigated both experimentally and numerically using the DEM in order to evaluate the correspondence. Furthermore, the influence of sliding and rolling friction, and shear rate on the elastic quasi-static and inertial non-collisional flow regimes was studied. Rolling friction was included to generate a realistic model granular system with respect to particle irregularities. Additionally, the effect of boundary conditions on the shear behaviour was investigated. The model parameters, particle size, effective density, and particle stiffness were chosen to match the experimental conditions.

Experimentally, an unexpected particle size dependence was observed where the shear resistance increased with particle size. This is inconsistent with the generally accepted flow behaviour i.e.

that flow is facilitated with increased particle size. Presumably this is explained by geometrical or kinetic factors causing mechanical interlocking, irregular shear planes or increased particle momentum.

Numerically, sliding and rolling friction were found to provide complementary resistance to shear. A critical sliding friction coefficient was identified at which a transition from the inertial non-collisional to the elastic quasi-static flow regime occurred. The magnitude of the critical sliding friction coefficient was dependent on rolling friction and shear rate. Hence, rolling friction did indeed influence the flow regimes by causing a transition from the inertial non-collisional to the elastic quasi-static regime. Rolling friction and shear rate independently increased the particle overlap and thus when combined largely enhanced the contact stresses. The increased contact stress was hypothesised to create more enduring contacts, thereby facilitating force chain formation and favouring elastic quasi-static flow.

Concerning the effect of boundary conditions, large simulated systems with the SBCs corresponded to smaller systems simulated using the LEBCs. With the LEBCs longer force chains may form in a small system due to the periodic boundaries. Inversely, a large system is required to enable a force chain of the same length due to the confining surfaces in the SBCs. However, simulations may be performed with both types of boundary conditions provided that the system size is accounted for.

Regarding the predictive capability of the DEM simulations the model displayed a satisfactory qualitative resemblance to experiments displaying the potential of the DEM to simulate granular shear behaviour. In addition, it was concluded that the presence of rolling friction is essential for an increased quantitative agreement. It is argued that a simulated system comprising non-spherical particles and an increased number of experimentally determined model parameters are necessary in order to improve the agreement between experimental and numerical results.

Acknowledgements

The authors wish to acknowledge Maria Similä for skilful experimental assistance and the Swedish Research Council (Project No. 621-2007-3854) for financial support.

References

- Aarons, L., Sundaresan, S., 2006. Shear flow of assemblies of cohesive and non-cohesive granular materials. *Powder Technol.* 169, 10-21.
- Aarons, L., Sundaresan, S., 2008. Shear flow of assemblies of cohesive granular materials under constant applied normal stress. *Powder Technol.* 183, 340-355.
- Bierwisch, C., Kraft, T., Riedel, H., Moseler, M., 2009. Three-dimensional discrete element models for the granular statics and dynamics of powders in cavity filling. *J. Mech. Phys. Solids* 57, 10-31.
- Campbell, C.S., 2002. Granular shear flows at the elastic limit. *J. Fluid Mech.* 465, 261-291.
- Campbell, C.S., 2005. Stress-controlled elastic granular shear flows. *J. Fluid Mech.* 539, 273-297.
- Campbell, C.S., 2006. Granular material flows - An overview. *Powder Technol.* 162, 208-229.
- Campbell, C.S., 2011. Elastic granular flows of ellipsoidal particles. *Physics of Fluids* 23, 013306.
- Carr, R.L., 1965. Evaluating flow properties of solids. *Chem. Eng.-New York* 72, 69-72.
- Castellanos, A., 2005. The relationship between attractive interparticle forces and bulk behaviour in dry and uncharged fine powders. *Adv. Phys.* 54, 263-376.
- Cundall, P.A., Strack, O.D.L., 1979. A discrete numerical model for granular assemblies. *Géotechnique* 29, 47-65.

- Datta, A., Mishra, B.K., Das, S.P., Sahu, A., 2008. A DEM analysis of flow characteristics of noncohesive particles in hopper. *Mater. Manuf. Process.* 23, 196-203.
- Eriksson, M., Nyström, C., Alderborn, G., 1993. The use of air permeametry for the assessment of external surface area and sphericity of pelletized granules. *International Journal of Pharmaceutics* 99, 197-207.
- European Federation of Chemical Engineering, 1989. Standard shear testing technique for particulate solids using the Jenike shear cell. The Institution of Chemical Engineers.
- Hartl, J., Ooi, J.Y., 2008. Experiments and simulations of direct shear tests: porosity, contact friction and bulk friction. *Granular Matter* 10, 263-271.
- Hirano, M., 2006. Atomistics of friction. *Surf. Sci. Rep.* 60, 159-201.
- Ji, S.Y., Hanes, D.M., Shen, H.H., 2009. Comparisons of physical experiment and discrete element simulations of sheared granular materials in an annular shear cell. *Mech. Mater.* 41, 764-776.
- Johansson, B., Wikberg, M., Ek, R., Alderborn, G., 1995. Compression behaviour and compactability of microcrystalline cellulose pellets in relationship to their pore structure and mechanical properties. *Int. J. Pharm.* 117, 57-73.
- Ketterhagen, W.R., Ende, M.T.A., Hancock, B.C., 2009. Process Modeling in the Pharmaceutical Industry using the Discrete Element Method. *J. Pharm. Sci.* 98, 442-470.
- Krupp, H., 1967. Particle adhesion theory and experiment. *Adv. Colloid Interface Sci.* 1, 111-239.
- Latzel, M., Luding, S., Herrmann, H.J., 2000. Macroscopic material properties from quasi-static, microscopic simulations of a two-dimensional shear-cell. *Granular Matter* 2, 123-135.
- Lees, A.W., Edwards, S.F., 1972. Computer study of transport processes under extreme conditions. *J. Phys. Part C Solid* 5, 1921-1929.
- McCarthy, J.J., Jasti, V., Marinack, M., Higgs, C.F., 2010. Quantitative validation of the discrete element method using an annular shear cell. *Powder Technol.* 203, 70-77.
- Nedderman, R.M., 1992. *Static and Kinematics of Granular Materials*, first ed. Cambridge university press, Cambridge.
- Persson, A.-S., Alderborn, G., Frenning, G., 2011. Flowability of surface modified pharmaceutical granules: A comparative experimental and numerical study. *Eur. J. Pharm. Sci.* 42, 199-209.
- Persson, A.-S., Frenning, G., 2012. An experimental evaluation of the accuracy to simulate granule bed compression using the discrete element method. *Powder Technol.* 219, 249-256.
- Savage, S.B., Sayed, M., 1984. Stresses developed by dry cohesionless granular materials sheared in an annular shear cell. *J. Fluid Mech.* 142, 391-430.
- Silbert, L.E., Ertaş, D., Grest, G.S., Halsey, T.C., Levine, D., Plimpton, S.J., 2001. Granular flow down an inclined plane: Bagnold scaling and rheology. *Physical Review E* 64, 051302.
- Tykhoniuk, R., Tomas, J., Luding, S., Kappl, M., Heim, L., Butt, H.J., 2007. Ultrafine cohesive powders: From interparticle contacts to continuum behaviour. *Chem. Eng. Sci.* 62, 2843-2864.
- Wensrich, C.M., Katterfeld, A., 2012. Rolling friction as a technique for modelling particle shape in DEM. *Powder Technol.* 217, 409-417.
- Wikberg, M., Alderborn, G., 1990. Compression characteristics of granulated materials II. Evaluation of granule fragmentation during compression by tablet permeability and porosity measurements. *International Journal of Pharmaceutics* 62, 229-241.
- Zhou, Y.C., Wright, B.D., Yang, R.Y., Xu, B.H., Yu, A.B., 1999. Rolling friction in the dynamic simulation of sandpile formation. *Physica A* 269, 536-553.

Zhou, Y.C., Xu, B.H., Yu, A.B., Zulli, P., 2001. Numerical investigation of the angle of repose of monosized spheres. *Phys. Rev. E* 64, 021301.

Figures

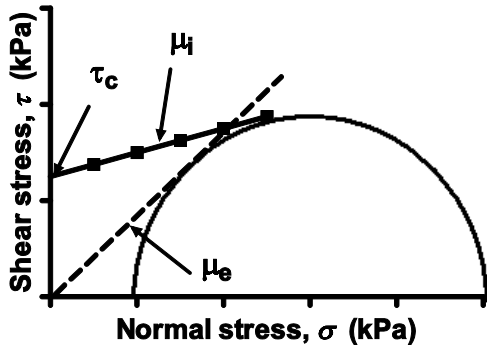


Figure 1: Schematic description of the yield locus (solid line) from which the cohesion (τ_c) and the internal friction coefficient (μ_i) are determined from the intercept and the slope respectively. The effective friction coefficient (μ_e) is determined from the slope of the effective yield locus (dashed line) that passes through the origin and is tangent to the large Mohr circle.

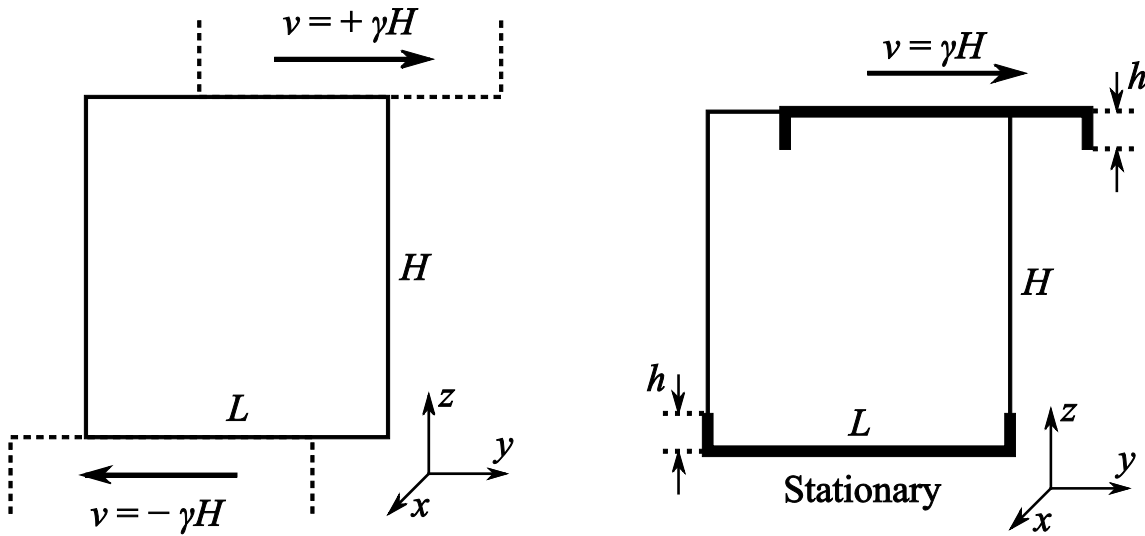
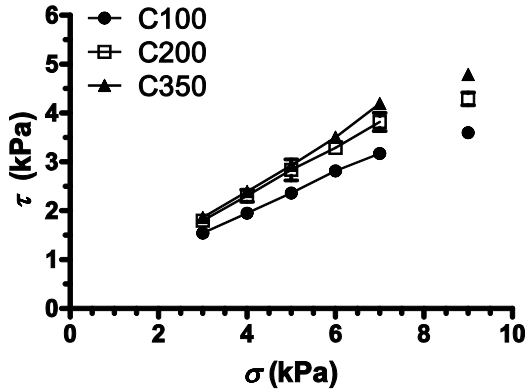


Figure 2: Illustration of the geometric setup used in the simulations: Lees–Edwards boundary conditions (left) and standard boundary conditions (right).

a)



b)

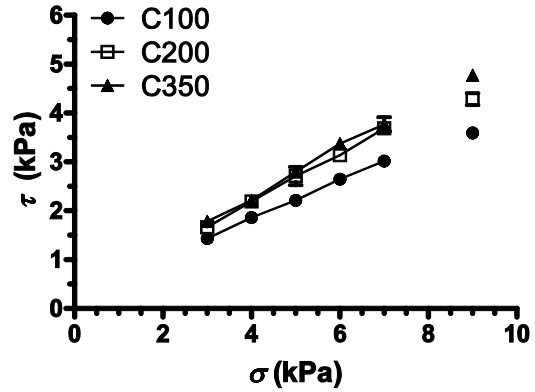
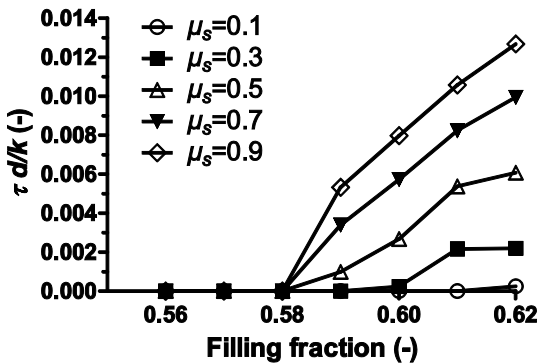


Figure 3: Yield loci for C100, C200, and C350. Data derived from a) the maximum detectable shear stress and b) the average shear stress during steady state.

a)



b)

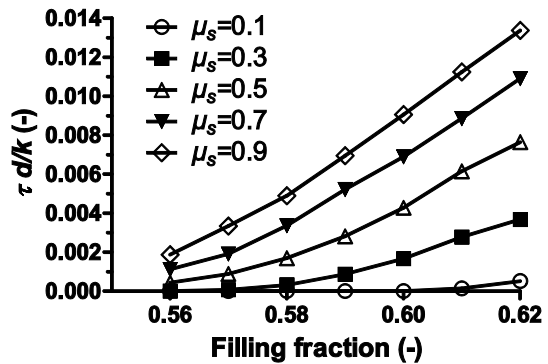


Figure 4: Shear stress as a function of filling fraction for varying sliding friction coefficients (μ_s). Simulations were performed at $\gamma = 0.01 \text{ ms}^{-1}$ for systems a) without rolling friction ($\mu_r=0$) and b) with rolling friction ($\mu_r=0.1$).

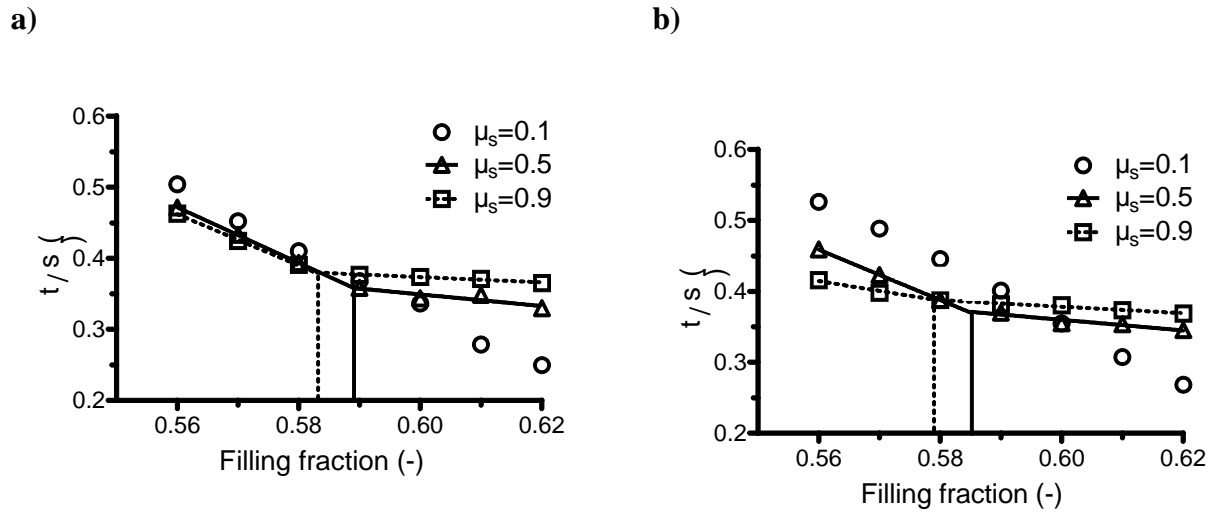


Figure 5: The apparent bulk friction (τ/σ) as a function of filling fraction for three sliding friction coefficients (μ_s) for systems a) without rolling friction ($\mu_r=0$) and b) with rolling friction ($\mu_r=0.1$). Simulations were performed at $\gamma = 0.01 \text{ ms}^{-1}$. The critical filling fractions were determined from the intersection of two regression lines.

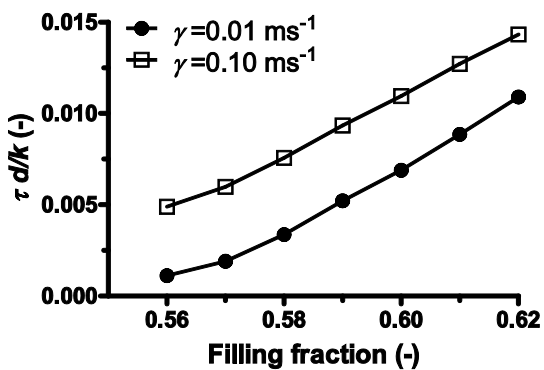


Figure 6: The generation of shear stress at varying shear rate (γ). Simulations were performed with sliding friction=0.7 and rolling friction=0.1.

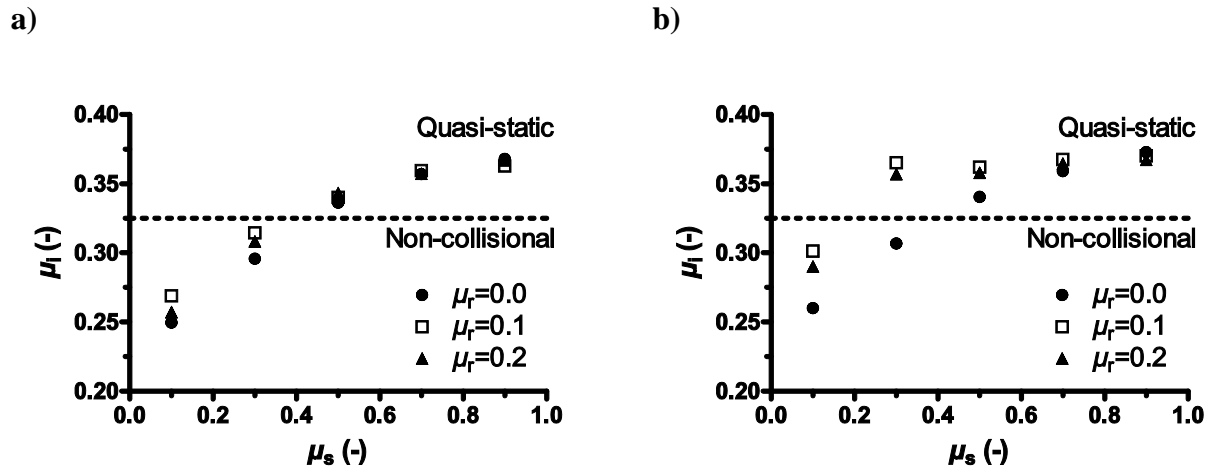


Figure 7: The simulated internal friction coefficient (μ_i) as a function of the sliding friction coefficient (μ_s) for systems with and without rolling friction (μ_r). Shearing was performed at a rate of a) $\gamma = 0.01 \text{ ms}^{-1}$ and b) $\gamma = 0.1 \text{ ms}^{-1}$.

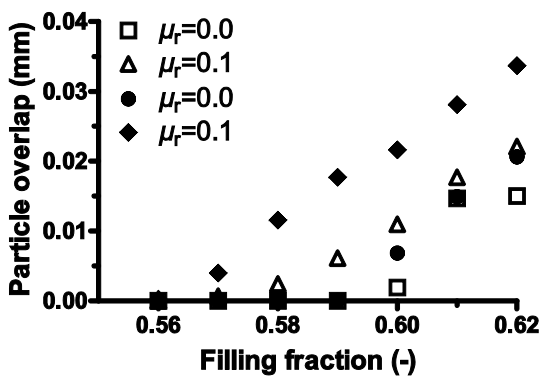


Figure 8: The dependence of the particle overlap on rolling friction (μ_r) and shear rate (γ) for simulations performed with sliding friction=0.3. The open symbols represent shearing at $\gamma = 0.01 \text{ ms}^{-1}$ and the closed symbols represent shearing at $\gamma = 0.1 \text{ ms}^{-1}$.

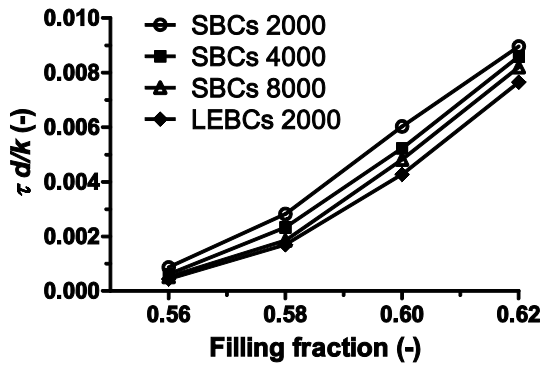


Figure 9: The effect of boundary conditions and system size on the shear stress. Simulations were performed using standard boundary conditions (SBCs) and Lees-Edwards boundary conditions (LEBCs) for the indicated number of particles.

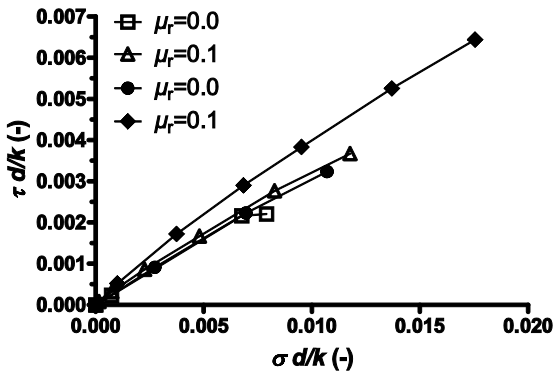


Figure 10: The simulated yield loci obtained from systems with sliding friction = 0.3 and varying rolling friction (μ_r). The open symbols represent shearing at $\gamma = 0.01 \text{ ms}^{-1}$ and the closed symbols represent shearing at $\gamma = 0.1 \text{ ms}^{-1}$.

Tables

Table 1: Granule characteristics. Standard deviations are given in parenthesis.

<i>Material</i>	d_{50} (μm) ^a	ρ_{eff} (g/cm^3) ^c	S_A (cm^{-1}) ^d	ρ_{bulk} (g/cm^3) ^e	ρ_{tap} (g/cm^3) ^f	CI (%) ^g
C100	170.1 (-)	1.45 (0.01)	399.8 (5.7)	0.78 (0.01)	0.91 (0.01)	14.7 (0.58)
C200	317.2 (-) ^b	1.46 (0.03)	215.9 (1.2)	0.82 (0.01)	0.91 (0.01)	10.0 (0.00)
C350	442.8 (-) ^b	1.45 (0.00)	150.8 (2.7)	0.84 (0.02)	0.92 (0.01)	9.3 (1.15)

^a Median particle diameter.

^b Obtained from (Persson and Frenning, 2012).

^c Effective granule density ($n=3$).

^d Volume specific external surface area ($n=3$).

^e Poured bulk density ($n=3$).

^f Tapped bulk density ($n=3$).

^g Carr's compressibility index ($n=3$).

Table 2: Shear properties derived from maximum shear stress. Standard deviations are given in parenthesis.

<i>Material</i>	τ_c (kPa) ^a	μ_i (-) ^b	μ_e (-) ^c
C100	0.31 (0.03)	0.41 (0.01)	0.45 (0.01)
C200	0.30 (0.13)	0.50 (0.03)	0.54 (0.02)
C350	0.09 (0.03)	0.58 (0.01)	0.59 (0.01)

^a Cohesion ($n=3$).

^b Internal friction coefficient ($n=3$).

^c Effective friction coefficient ($n=3$).

Table 3: Shear properties derived from average shear stress at steady state. Standard deviations are given in parenthesis.

<i>Material</i>	τ_c (kPa) ^a	μ_i (-) ^b	μ_e (-) ^c
C100	0.25 (0.02)	0.40 (0.00)	0.43 (0.00)
C200	0.17 (0.07)	0.50 (0.02)	0.53 (0.02)
C350	0.16 (0.10)	0.53 (0.02)	0.55 (0.01)

^a Cohesion ($n=3$).

^b Internal friction coefficient ($n=3$).

^c Effective friction coefficient ($n=3$).

Table 4: Critical filling fractions indicating where the flow regime transition occurs.

μ_s^a (-)	Critical filling fraction (-)	
	$\mu_r^b=0$	$\mu_r=0.1$
0.1 ^c	-	-
0.3	0.596	0.594
0.5	0.589	0.585
0.7	0.585	0.581
0.9	0.583	0.579

^a Sliding friction coefficient.

^b Rolling friction coefficient.

^c Shearing occurs in the inertial non-collisional flow regime for all investigated filling fractions.

Table 5: Internal friction coefficients obtained from the simulations.

μ_s^c (-)	μ_i^a ($\gamma^b = 0.01 \text{ ms}^{-1}$)		
	$\mu_r^d=0$	$\mu_r=0.1$	$\mu_r=0.2$
0.1	0.250	0.269	0.257
0.3	0.296	0.314	0.308
0.5	0.336	0.340	0.343
0.7	0.357	0.359	0.357
0.9	0.368	0.363	0.367

μ_i ($\gamma = 0.1 \text{ ms}^{-1}$)			
0.1	0.260	0.301	0.290
0.3	0.307	0.365	0.357
0.5	0.340	0.362	0.358
0.7	0.359	0.367	0.364
0.9	0.373	0.370	0.367

^a Internal friction coefficient.

^b Shear rate.

^c Sliding friction coefficient.

^d Rolling friction coefficient.